Enhanced reversibility of the magnetoelastic transition in $(Mn,Fe)_2(P,Si)$ alloys via minimizing the transition-induced elastic strain energy

Miao, Xuefei; Gong, Yong; Zhang, Fengqi; You, Yurong; Caron, Luana; Qian, Fengjiao; Xu, Feng; van Dijk, Niels; Brück, Ekkes; More Authors

DOI
10.1016/j.jmst.2021.05.087

Publication date
2022

Document Version
Accepted author manuscript

Published in
Journal of Materials Science and Technology

Enhanced reversibility of the magnetoelastic transition in $(Mn,Fe)_2(P,Si)$ alloys via minimizing the transition-induced elastic strain energy

Xuefei Miao [a,*], Yong Gong [a], Fengqi Zhang [b], Yurong You [a], Luana Caron [c], Chin-Wei Wang [d], Fengjiao Qian [e], Yujing Zhang [a], Yuanyuan Gong [a], Feng Xu [a,**], Niels van Dijk [b], Ekkes Brück [b]

[a] *MIIT Key Laboratory of Advanced Metallic and Intermetallic Materials Technology, School of Materials Science and Engineering, Nanjing University of Science and Technology, 210094 Nanjing, China*

[b] *Fundamental Aspects of Materials and Energy, Department of Radiation Science and Technology, Delft University of Technology, Mekelweg 15, 2629 JB Delft, The Netherlands*

[c] *Department of Physics, Bielefeld University, 33501 Bielefeld, Germany*

[d] *National Synchrotron Radiation Research Center, 30076 Hsinchu, Taiwan*

[e] *College of Physics, Nanjing University of Aeronautics and Astronautics, 210016 Nanjing, China*

[*] Corresponding author. E-mail address: xuefeimiao@njust.edu.cn (X.M.)

[**] Corresponding author. E-mail address: xufeng@njust.edu.cn (F.X.)

Abstract

Magnetocaloric materials undergoing reversible phase transitions are highly desirable for magnetic refrigeration applications. $(Mn,Fe)_2(P,Si)$ alloys exhibit a giant magnetocaloric effect accompanied by a magnetoelastic transition, while the noticeable irreversibility causes drastic degradation of the magnetocaloric properties during consecutive cooling cycles. In the present work, we performed a comprehensive study on the magnetoelastic transition of the $(Mn,Fe)_2(P,Si)$ alloys by high-resolution transmission electron microscopy, *in situ* field- and temperature-dependent neutron powder diffraction as well as density functional theory calculations (DFT). We found a generalized relationship between the thermal hysteresis and the transition-induced elastic strain energy for the $(Mn,Fe)_2(P,Si)$ family. The thermal hysteresis was greatly reduced from 11 to 1 K by a mere 4 at.% substitution of Fe by Mo in the $Mn_{1.15}Fe_{0.80}P_{0.45}Si_{0.55}$ alloy. This reduction is found to be due to a strong reduction in the

transition-induced elastic strain energy. The significantly enhanced reversibility of the magnetoelastic transition leads to a remarkable improvement of the reversible adiabatic temperature, compared to the parent alloy. Based on the DFT calculations and the neutron diffraction experiments, we also elucidated the underlying mechanism of the tunable transition temperature for the $(Mn,Fe)_2(P,Si)$ family, which can essentially be attributed to the strong competition between covalent bonding and ferromagnetic exchange coupling. The present work provides not only a new strategy to improve the reversibility of a first-order magnetic transition but also essential insight into the electron-spin-lattice multi-coupling in giant magnetocaloric materials.

Keywords

Magnetocaloric effect; $(Mn,Fe)_2(P,Si)$; Hysteresis; Neutron diffraction;

1. Introduction

The magnetocaloric effect (MCE) couples a change in magnetic field to a change in temperature of a material and thereby lays the foundation for magnetic refrigeration, a cutting-edge cooling technology with merits of high energy efficiency and low environmental impact [1, 2]. A giant MCE is usually accompanied by first-order magnetic transitions (FOMTs), as observed in $Gd_5(Si,Ge)_4$ [3], $(Mn,Fe)_2(P,Si)$ [4], $La(Fe,Si)_{13}$ [5, 6], MnMX [7, 8] and NiMn-based Heusler alloys [9, 10]. The FOMT is tied to either a structural transformation (i.e. magnetostructural transition) or to discontinuous changes in the unit-cell parameters with a conserved symmetry of the lattice (i.e. magnetoelastic transition). Therefore, a concrete strategy for seeking giant MCE materials is to screen materials with magnetostructural or magnetoelastic transitions. Nevertheless, the irreversibility of the magnetostructural or magnetoelastic transitions, manifesting itself in thermal and field hysteresis, causes a drastic reduction of the MCE during consecutive cooling cycles [11, 12]. Consequently, understanding and eliminating this hysteresis is crucial for the commercialization of this revolutionary cooling technology.

According to Landau theory [13-15], several local minima are present in the Gibbs free energy of a FOMT system in the vicinity of the transition. The selected local minimum depends on the thermal and field history of the system. As a result, the FOMT is controlled by different energy barriers between the local and global minima in the Gibbs free energy during cooling and heating (or increasing and decreasing the magnetic field), which causes thermal (or magnetic) hysteresis. Apart from this intrinsic hysteresis, structural discontinuities like dislocations, second phase particles and micro-cracks may affect at the irreversible processes in the FOMT [16-18]. Structural defects may localloy facilitate the nuclation of the new phase (heterogeneous nucleation), resulting in a reduction of the hysteresis, or may cause a pinning of the moving interface during the growth of the new phase, resulting in an increase of the hysteresis (extrinsic hystersis).

Different ways of minimizing the hysteresis have been proposed, which can be separated into five main categories: (i) tailoring the order of the transition [19-21]; (ii) improving the structural compatibility between phases [22-27]; (iii) introducing nano-precipitations or multi-

scale structural defects [28-38]; (iv) tuning the kinetics of the transition [39, 40]; (v) driving the transition via multi-stimuli [10, 41]. Unlike the first-order transition, the second-order transition is completely reversible without hysteresis, although the MCE is moderate. A balance between the MCE and the reversibility can be achieved by tuning the transition towards the tricritical point, i.e. the crossover from first to second order. At the tricritical point, materials exhibit no hysteresis but retain a giant MCE, as demonstrated in the MnCo(Ge,Si) [19] and Tb_5SiGe_2 [20] alloys. As revealed by *in situ* neutron diffraction [42] and Hall-probe imaging measurements [19], the first-order magnetic transition is driven by the nucleation and growth of the product phase from the parent phase. It has been found that the NiTi-based shape memory alloys [23], NiMn-based Heusler alloys [24-26] and MnNiGe-based alloys [27] exhibit low hysteresis when the product and the parent phases satisfy certain geometric compatibility conditions. In addition, the presence of nano-precipitations [28-31], local atomic disorder [32-34] and nano-pores [35] has also been proven to lower the nucleation barrier and reduce the hysteresis. At the mesoscopic scale, the partial removal of grain boundaries [36] and the introduction of micro-cracks [37] or micro-pores [38] can also lead to smaller hysteresis since the transition-induced stress is easier to be released. Apart from tuning the giant MCE material itself, the hysteresis can finally be reduced by optimizing the external stimuli, e.g., a small sweeping rate of the driving field [39, 40] and the utilization of multicaloric cycles driven by magnetic-pressure [10] or magnetic-electric [41] multi-stimuli.

Extensive studies have been carried out to reduce the hysteresis of the $(Mn,Fe)_2(P,Si)$ alloys that show great application potential due to the giant MCE and the abundance of the constituent elements. Without understanding the underlying mechanism causing the hysteresis, the development of superior $(Mn,Fe)_2(P,Si)$ alloys is largely based on trial and error. In the present work, we employed high-resolution transmission electron microscope (TEM), *in situ* field- and temperature-dependent neutron powder diffraction (NPD) as well as density functional theory calculations (DFT) to explore the first-order magnetoelastic transition in the $(Mn,Fe)_2(P,Si)$ alloys. We found a generalized relationship between the thermal hysteresis and the transition-induced elastic strain energy for the $(Mn,Fe)_2(P,Si)$ family, which offers new guidance for optimizing this material system and other giant MCE materials.

2. Experimental details

2.1 Sample synthesis

$Mn_{1.15}Fe_{0.80-x}Mo_xP_{0.45}Si_{0.55}$ (x = 0, 0.01, 0.02 and 0.04) polycrystalline alloys were prepared by high-energy ball milling. The off-stoichiometry of the nominal compositions, i.e. slight deficiency in the metal elements, was intended to reduce the Fe_3Si-type secondary phase [17, 43]. The calculated amount of Mn, Fe, Mo, red P and Si powders with a purity higher than 99.8 wt.% was mixed and ball milled at a speed of 400 rpm for 10 h. The fine powders after ball milling were pressed into tablets at room temperature, sealed into quartz ampoules in vacuum and annealed at 1373 K for 40 h before being quenched into iced water.

2.2 Crystal and magnetic structure characterization

Neutron powder diffraction measurements were performed on the high-intensity powder diffractometer (WOMBAT) [44] at the OPAL Reactor (Lucas Heights, Australia). The $Mn_{1.15}Fe_{0.80-x}Mo_xP_{0.45}Si_{0.55}$ powders were loaded into a vanadium can and fixed with aluminum foils. For temperature-dependent measurements in zero field, a top loading cryofurnace was used and the data were collected between 4 and 350 K upon warming. For magnetic field-dependent measurements, a vertical field magnet was used, which can provide magnetic fields up to 9 T between 1.5 and 300 K. To avoid any temperature- or field-history effect on the field-dependent measurements, the samples were always zero-field cooled from 300 K to the specific measuring temperature before starting the field-dependent measurements. The incident neutron wavelength was 1.542047 and 2.410418 Å for the temperature- and field-dependent measurements, respectively.

X-ray powder diffraction (XRD) measurements were performed on a PANalytical X-pert Pro diffractometer equipped with an Anton Paar TTK450 low-temperature chamber, which allows temperature-dependent measurements. Crystallographic and magnetic structure refinement of the NPD and XRD patterns was performed using Fullprof's [45] implementation of the Rietveld refinement method.

2.3 Microstructure observation and composition analysis

Surface morphology and compositional analysis of the samples were characterized using

a field-emission scanning electron microscope (SEM, ZEISS, Sigma 500) equipped with an X-ray energy dispersive spectroscope (EDS).

Atomic-resolution structural characterization was performed on an FEI Titan Themis 80-300 transmission electron microscope, equipped with two (probe and image) aberration correctors and a highly efficient (4 quadrant) EDS. This TEM offers a maximum resolution of 0.06 nm in the high-angle annular dark-field (HAADF) scanning TEM (STEM) mode. The TEM specimen was prepared in a focused ion beam system (FIB, FEI, Helios Nanolab 600i) using the lift-out method.

2.4 Magnetic characterization

The magnetic properties were measured in a superconducting quantum interference device magnetometer (SQUID, Quantum Design MPMS 5XL) using the reciprocating sample option (RSO) mode. Reversible ΔT_{ad} of the $Mn_{1.15}Fe_{0.80-x}Mo_xP_{0.45}Si_{0.55}$ (x = 0, 0.01, 0.02 and 0.04) alloys was measured in the temperature range $240 \leq T \leq 310$ K in a homemade device [46, 47] at Delft University of Technology, the Netherlands.

2.5 Electronic structure calculations

Density functional theory calculations were performed on the $(Mn,Fe,Mo)_2(P,Si)$ alloys using the Vienna ab initio simulation package (VASP) [48]. Perdew-Burke-Ernzerhof (PBE) pseudopotentials with generalized gradient approximation (GGA) were implemented in exchange correlation functions. A plane-wave cutoff energy of 500 eV and a Γ-centered k-point mesh of 9×9×9 were taken. A 2×2×2 supercell was constructed, where one of the 24 Mn (or Fe) atoms at the 3g (or 3f) sites was replaced by the Mo atom, corresponding to about 4% Mo substitution for the Mn or Fe in the $(Mn,Fe)_2(P,Si)$ alloys. The unit-cell parameters of the supercell were taken from the neutron diffraction results of the $Mn_{1.15}Fe_{0.76}Mo_{0.04}P_{0.45}Si_{0.55}$ sample measured at 5 K.

Electron localization function (ELF) [49], indicating the strength of chemical bonds between neighboring atoms, was calculated for the $(Mn,Fe)_2(P,Si)$ alloy in both paramagnetic (PM) and ferromagnetic (FM) states. The PM state was modeled by a 1×1×2 supercell, which is double the FM supercell with antiparallel moment ordering along the c axis of the hexagonal

structure to make the net moment zero. For simplicity, the 3*g*, 3*f*, 2*c* and 1*b* sties in both supercells were fully occupied by the Mn, Fe, Si and P atoms, respectively.

3. Results and discussion

3.1 Magnetic properties

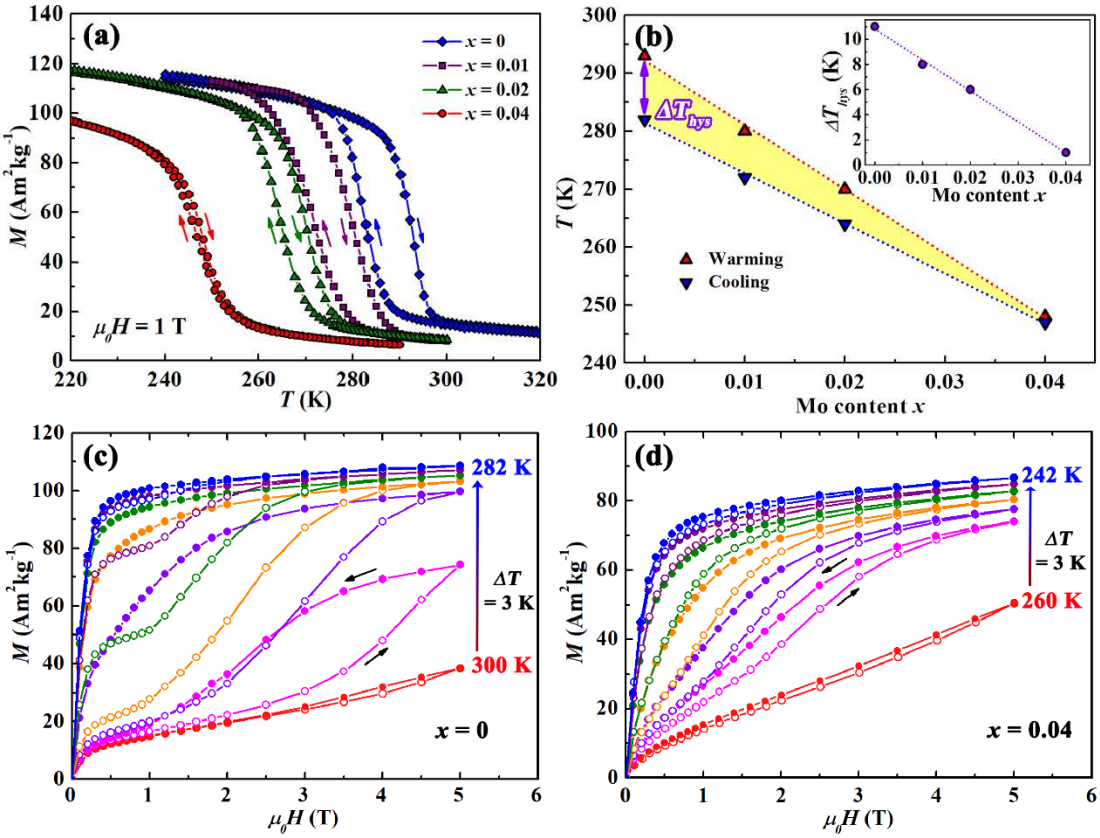

Fig. 1. (a) Temperature-dependent magnetization measured in 1 T for the $Mn_{1.15}Fe_{0.80-x}Mo_xP_{0.45}Si_{0.55}$ alloys. (b) Curie temperature as a function of the Mo content derived from the thermomagnetic curves. The dependence of thermal hysteresis on the Mo content is shown in the inset of (b). Isothermal magnetization/demagnetization curves for the x = 0 (c) and 0.04 (d) alloys.

Fig. 1(a) shows the magnetization (M) measured at various temperatures (T) for the $Mn_{1.15}Fe_{0.80-x}Mo_xP_{0.45}Si_{0.55}$ alloys. The Curie temperature (T_C) of the magnetoelastic transition can be determined from the M-T curves, which corresponds to the temperature where the $|dM/dT|$ shows a maximum. The T_C values of the cooling and warming branches for all the $Mn_{1.15}Fe_{0.80-x}Mo_xP_{0.45}Si_{0.55}$ alloys are plotted in Fig. 1(b). The Mo-free alloy shows a considerable difference in the T_C between the cooling and warming branches, indicating a large thermal hysteresis (ΔT_{hys}) of the magnetoelastic transition. By partial substitution of Fe by Mo,

the T_C decreases almost linearly at a rate of 11.1(3) and 8.7(3) K/at.% Mo substitution for the warming and cooling branches, respectively. The faster decrease in the T_C of the warming branch than that of the cooling branch leads to a smaller ΔT_{hys} in the samples with higher Mo contents. ΔT_{hys} also shows a linear dependence on the Mo content (see the inset of Fig. 1(b)). The value of ΔT_{hys} is significantly reduced from 11 to 1 K (i.e. by about 91%) via a mere 4 at.% Mo substitution for Fe in the $Mn_{1.15}Fe_{0.80}P_{0.45}Si_{0.55}$ alloy.

Figs. 1(c) and 1(d) present the isothermal magnetization/demagnetization curves measured at temperatures close to the T_C of the Mo-free and x = 0.04 alloys, respectively. The field-induced PM-to-FM transition can be observed in both alloys, manifested by the rapid increase in the magnetization above a critical magnetic field (e.g., above 3 T in the *M-H* curve collected at 297 K for the Mo-free alloy shown in Fig. 1(c)). Both alloys display a magnetic hysteresis, which characterizes the irreversibility of the field-induced PM-to-FM transition. Nevertheless, the magnetic hysteresis is greatly reduced in the x = 0.04 alloy compared to the Mo-free alloy. Therefore, the x = 0.04 alloy shows both smaller thermal and magnetic hysteresis than the Mo-free alloy, suggesting an enhanced reversibility of the magnetoelastic transition after Mo substitution.

3.2 *In situ* field-dependent neutron diffraction studies

We further performed *in situ* field-dependent neutron diffraction experiments to quantitatively study the reversibility of the magnetoelastic transition in the x = 0.04 alloy. Fig. 2(a) shows the neutron diffraction patterns collected at 257 K (slightly higher than T_C) from the x = 0.04 sample. The peaks at the 2θ of 41.0° and 46.2° in the zero-field diffraction pattern are indexed as the (001) and (110) Bragg peaks of the Fe_2P-type hexagonal structure, respectively. With an increase in the magnetic field from 0 to 9 T, two new peaks centered at 41.6° and 46.0° appear and grow at the expense of the original peaks centered at 41.0° and 46.2°, respectively. According to the Rietveld refinement, the two new peaks also belong to the Fe_2P-type hexagonal structure, but with different lattice parameters. This reveals a magnetic field-driven magnetoelastic transition, where the PM-to-FM transition is coupled to discontinuous changes in the lattice parameters. Upon removal of the magnetic field, a slightly different diffraction pattern was obtained as compared to the original zero-field diffraction pattern, suggesting a

partial irreversibility of the magnetoelastic transition during the first field cycle. When the magnetic field is applied for the second time, the diffraction patterns overlap with those collected at the same field during the first field cycle. Additionally, the zero-field diffraction patterns collected before and after the second field cycle are almost identical, suggesting a complete reversibility of the magnetoelastic transition during the second field cycle.

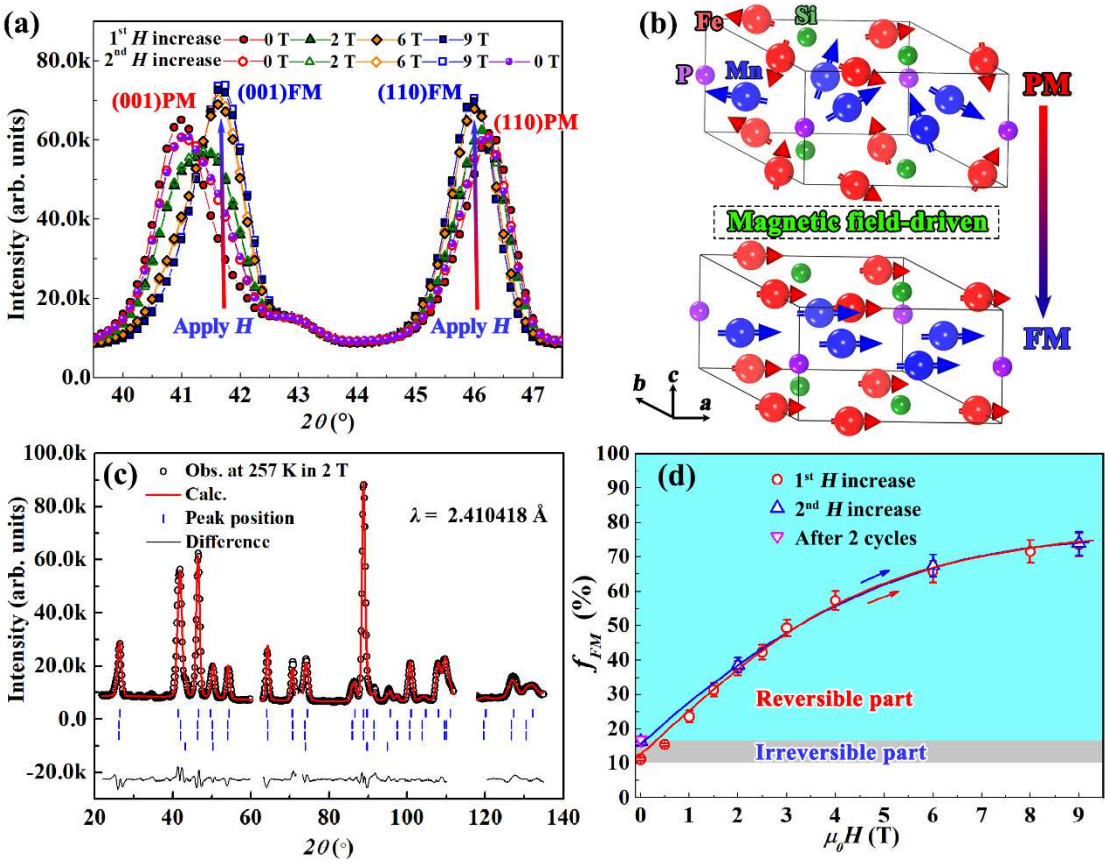

Fig. 2. (a) *In situ* field-dependent neutron diffraction patterns collected at 257 K from the $Mn_{1.15}Fe_{0.76}Mo_{0.04}P_{0.45}Si_{0.55}$ alloy. (b) Schematic illustration of the field-induced magnetoelastic transition in the $(Mn,Fe)_2(P,Si)$ alloys. (c) Rietveld refinement of the neutron diffraction pattern collected in 2 T at T = 257 K after zero-field cooling from 300 K. Vertical lines indicate the peak positions (from top to bottom) of the PM $(Mn,Fe)_2(P,Si)$ phase, the nuclear structure of the FM $(Mn,Fe)_2(P,Si)$ phase, the magnetic structure of the FM $(Mn,Fe)_2(P,Si)$ phase, and the Fe_3Si-type impurity phase, respectively. Note that the diffraction peaks from the magnet are excluded from the diffraction patterns. (d) The volume fraction of the transformed FM phase (f_{FM}) derived from neutron diffraction patterns during the first 2 field cycles at 257 K after zero-field cooling from 300 K.

The fraction of the transformed FM phase (f_{FM}) in different magnetic fields can be determined from the Rietveld refinement of the neutron diffraction patterns (see Fig. 2(c) as an example). Fig. 2(d) shows the evolution of the fraction of the FM phase with respect to the

applied magnetic field. Upon cooling from 300 to 257 K in zero field, about 11.2% of the $Mn_{1.15}Fe_{0.76}Mo_{0.04}P_{0.45}Si_{0.55}$ alloy is in the FM state (i.e. $f_{FM} \approx 11.2\%$). With an increase in the magnetic field, f_{FM} rises quickly and reaches approximately 73.6% at 9 T, manifesting a field-driven PM-to-FM transition. Upon removing the magnetic field, the inverse transition occurs and f_{FM} drops back to 16.4%. As a result, slightly more (about 5.3%) FM phase is present at zero field after the first field cycle, corresponding to the irreversible part of the transition. When applying the field for the second time, f_{FM} increases again and reaches roughly the same values at 2, 6 and 9 T as observed during the first field cycle. After the second field cycle, f_{FM} decreases to 16.9% at zero field, which is very close to the zero-field f_{FM} value of 16.4% before the second field cycle. Consequently, the field-dependent neutron diffraction experiments reveal an excellent reversibility of the $Mn_{1.15}Fe_{0.76}Mo_{0.04}P_{0.45}Si_{0.55}$ alloy, which is desirable for magnetic refrigeration applications driven by a cyclic magnetic field.

3.3 Magnetocaloric properties

For magnetic refrigeration applications, two primary thermodynamic parameters are of equal importance to the magnetocaloric materials, i.e. the isothermal entropy change (Δs_T) and the adiabatic temperature change (ΔT_{ad}) [2]. The former measures the maximum amount of heat that can be taken from a load in one cooling cycle, while the latter determines the maximum temperature span between a load and a heat sink.

The isothermal entropy change can be derived from isothermal magnetization measurements (as shown in Fig. 1(c) and 1(d)) based on Maxwell relations. It should be noted that the so-called “loop protocol” [50] was adopted in the isothermal magnetization measurements to avoid the thermal-history effect when a first-order phase transition is probed. Fig. 3(a) plots the temperature-dependent isothermal entropy change in a magnetic field change of 1 and 2 T for the $Mn_{1.15}Fe_{0.80-x}Mo_xP_{0.45}Si_{0.55}$ alloys. The Mo-free alloy demonstrates maximum Δs_T values of 8.0 and 16.3 $Jkg^{-1}K^{-1}$ in a field change of 1 and 2 T, respectively. With an increase in the Mo content, the maximum Δs_T value is slightly reduced. Nevertheless, the maximum Δs_T values of the $x = 0.04$ alloy are still at least twice as large as that of the benchmark magnetocaloric material Gd [51].

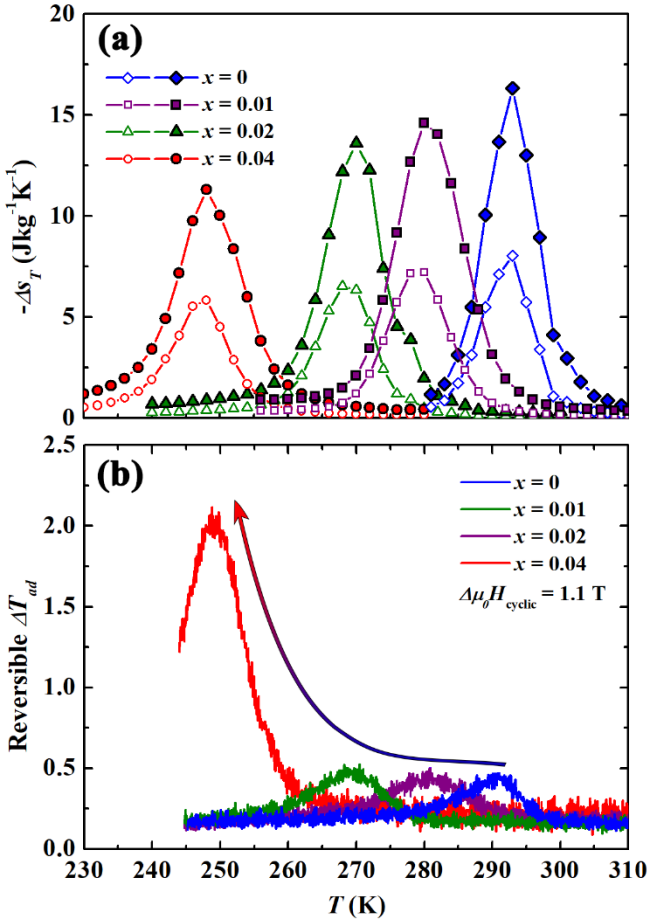

Fig. 3. (a) Isothermal entropy change in a field change of 1 (open symbols) and 2 T (solid symbols), and (b) reversible adiabatic temperature change in a cyclic field of 1.1 T for the $Mn_{1.15}Fe_{0.80-x}Mo_xP_{0.45}Si_{0.55}$ alloys.

The adiabatic temperature change associated with the magnetoelastic transition of the $Mn_{1.15}Fe_{0.80-x}Mo_xP_{0.45}Si_{0.55}$ alloys was directly measured by a Chromel-Constantan thermocouple in a homemade device [46, 47] at Delft University of Technology. The powdered samples were compressed in a capsule, which moved at a frequency of 0.1 Hz in and out of a magnetic field ($\mu_0 H$ = 1.1 T) generated by a permanent magnet. The reversible ΔT_{ad} at various temperatures is shown in Fig. 3(b). Although the Mo-free sample exhibits a giant magnetocaloric effect with a large Δs_T value, it displays a maximum reversible ΔT_{ad} of only 0.4 K in a cyclic field of 1.1 T. The relatively small reversible ΔT_{ad} is attributed to the large thermal and magnetic hysteresis of the magnetoelastic transition, as shown in Fig. 1. Benefiting from the significantly enhanced reversibility of the magnetoelastic transition, the x = 0.04 sample shows a large reversible ΔT_{ad} of more than 2.0 K, i.e. 5 times as large as that of the Mo-free alloy.

3.4 Micro- and atomic-scale structural characterization

The magnetic and magnetocaloric results indicate that partial replacement of the Fe by Mo in the $Mn_{1.15}Fe_{0.80}P_{0.45}Si_{0.55}$ alloys leads to a remarkable enhancement in the reversibility of the magnetoelastic transition. To understand the underlying mechanism, we performed micro- and atomic-scale structural characterization using SEM and TEM. Fig. 4 shows the SEM backscattered electrons (BSE) image and the corresponding EDS maps of the $Mn_{1.15}Fe_{0.76}Mo_{0.04}P_{0.45}Si_{0.55}$ alloy. Based on the SEM and EDS results, 3 different phases can be identified in the alloy, i.e. the $(Mn,Fe)_2(P,Si)$ main phase (marked as "A" in the SEM image), the (Fe,Si)-rich grain-boundary phase (marked as "B") and the dispersed Si-rich phase (marked by "C"). Obviously, the Mo atoms enter the main phase and not the impurity phases according to the EDS results (see Fig. 4(d)). It should be noted that the (Fe,Si)-rich grain-boundary phase and the dispersed Si-rich phase are present in all of the $Mn_{1.15}Fe_{0.80-x}Mo_xP_{0.45}Si_{0.55}$ (x = 0, 0.01, 0.02 and 0.04) samples, regardless of the Mo content.

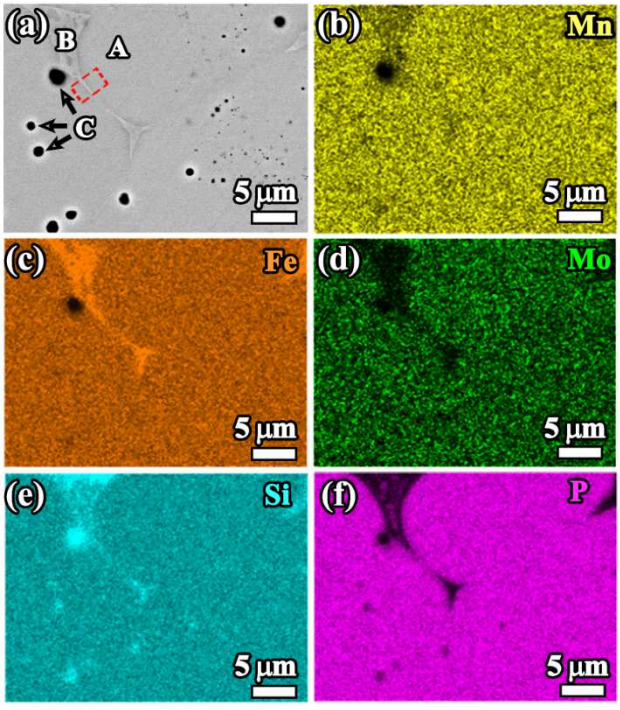

Fig. 4. (a) SEM BSE image and (b-f) the corresponding EDS maps of the $Mn_{1.15}Fe_{0.76}Mo_{0.04}P_{0.45}Si_{0.55}$ alloy.

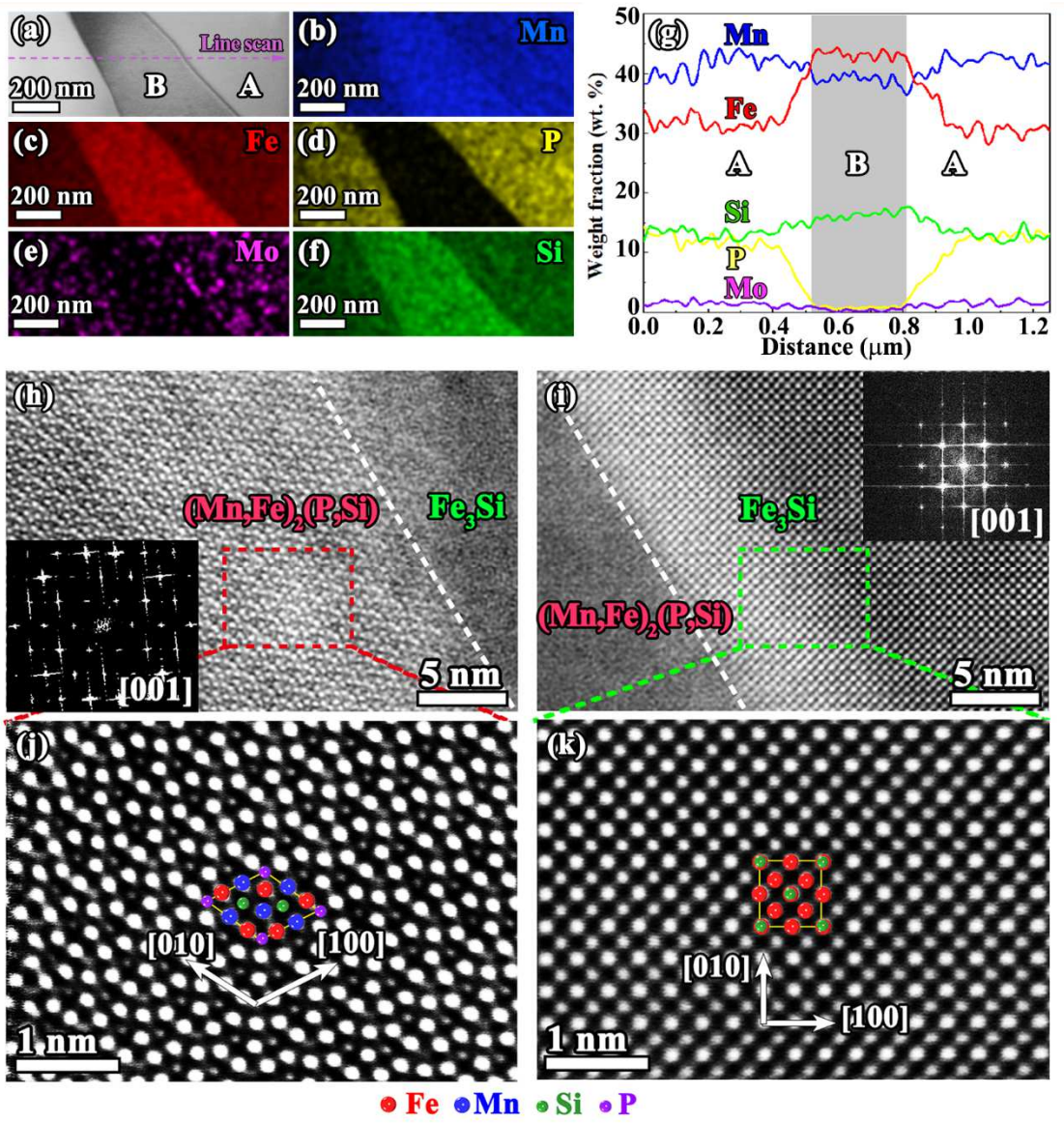

Fig. 5. (a) Bright-field TEM image and (b-f) the corresponding EDS maps for the $Mn_{1.15}Fe_{0.76}Mo_{0.04}P_{0.45}Si_{0.55}$ alloy. (g) Composition depth profile along the dashed lines in (a). STEM-HAADF images of the grain boundary area observed from the [001] zone axis of (h) the $(Mn,Fe)_2(P,Si)$ phase and (i) the [001] zone axis of the Fe_3Si-type phase. Insets in (h) and (i) are the corresponding FFT patterns of the $(Mn,Fe)_2(P,Si)$ and Fe_3Si-type phases, respectively. High-magnification STEM-HAADF images of (j) the $(Mn,Fe)_2(P,Si)$ main phase and (k) the Fe_3Si-type grain-boundary phase.

We further performed TEM analyses on the $Mn_{1.15}Fe_{0.76}Mo_{0.04}P_{0.45}Si_{0.55}$ alloy. A region near the ground boundary (enclosed by the dashed lines in Fig. 4(a)) was lifted out for the TEM observations using a FIB system. Figs. 5(a) displays the bright-field TEM image of the selected region with corresponding EDS maps shown in Figs. 5(b-f). The Mo atoms are well distributed in the main phase, in good agreement with the SEM-EDS results. The concentration profiles

across the grain boundary obtained from the EDS line-scan analysis (illustrated by the dashed arrow in Fig. 5(a)) were shown in Fig. 5(g). The average compositions of the main and the grain-boundary phases are $Mn_{1.08}Fe_{0.74}Mo_{0.03}P_{0.51}Si_{0.59}$ and $Fe_{1.34}Mn_{1.23}Si$, respectively, as derived from the EDS analysis. The measured composition of the main phase is close to the nominal composition despite the presence of a small amount of the Fe_3Si-type grain-boundary phase.

Figs. 5(h) and 5(i) display the STEM-HAADF images taken along the [001] zone axis of the $(Mn,Fe)_2(P,Si)$ main phase and the [001] zone axis the Fe_3Si-type grain-boundary phase, respectively. No nano- or micro-cracks were observed at the phase interfaces, which suggests that the formation of the Fe_3Si-type grain-boundary phase does not deteriorate the structural integrity of the $(Mn,Fe)_2(P,Si)$ main phase. Enlarged views of the atomic arrangement of the main and the grain-boundary phases are shown in Figs. 5(j) and 5(k), respectively. The $(Mn,Fe)_2(P,Si)$ main phase retains the Fe_2P-type hexagonal structure (space group *P-62m*) after the Mo substitution. No structural defects (e.g., dislocations, stacking faults, twins) were detected in the $(Mn,Fe,Mo)_2(P,Si)$ main phase.

Consequently, the micro- and atomic-scale structural analyses reveal that the Mo atoms have entered the $(Mn,Fe)_2(P,Si)$ main phase, which causes subtle structural variations of the hexagonal unit cell and results in a remarkable improvement in the reversibility of the magnetoelastic transition.

3.5 *In situ* temperature-dependent neutron diffraction studies

The influence of the Mo substitution on the structure and magnetoelastic phase transition of the $(Mn,Fe)_2(P,Si)$ alloy was further investigated by *in situ* temperature-dependent neutron diffraction experiments. Figs. 6(a) and 6(b) show the contour plots of the neutron diffraction patterns collected at different temperatures for the $Mn_{1.15}Fe_{0.80-x}Mo_xP_{0.45}Si_{0.55}$ alloys with $x = 0$ and 0.04, respectively. Both alloys exhibit discontinuous changes in the lattice parameters at the T_C, while the symmetry of the lattice is conserved. The higher intensity of the (001) peak at lower temperatures is due to the increased magnetic diffraction contribution. The magnetic and structural parameters of the $Mn_{1.15}Fe_{0.80-x}Mo_xP_{0.45}Si_{0.55}$ alloys can be derived from the Rietveld refinement of the neutron diffraction patterns (see Fig. 6(c) as an example). In the Fe_2P-type

hexagonal structure (space group *P-62m*), the Mn and Fe atoms prefer to occupy the 3*g* and 3*f* crystallographic sites, respectively [52]. Our DFT calculations estimated the total energy of -576.2855 and -575.9443 eV for the structural configurations with the Mo atoms entering the 3*g* and 3*f* sites, respectively, which predicts a preferential occupation of the Mo atoms at the 3*g* site. Our neutron diffraction data experimentally verify the DFT prediction based on the large difference in the coherent neutron-scattering length between Mn (-3.73 fm), Fe (9.45 fm), and Mo (6.715 fm). In the Mo-free alloy, the Mn (3*g* site) and Fe (3*f* site) moments derived from the neutron diffraction data are 2.55±0.16 and 1.69±0.16 μ_B, respectively, while those in the x = 0.04 alloy are 2.41±0.16 and 1.65±0.16 μ_B, respectively. Obviously, the non-magnetic Mo atoms entering the 3*g* site slightly reduces the average sublattice magnetic moment at the 3*g* site.

Figs. 6(d-e) show the thermal-evolution of the lattice parameters for the $Mn_{1.15}Fe_{0.80-x}Mo_xP_{0.45}Si_{0.55}$ alloys. Note that the lattice parameters of the x = 0 and 0.04 alloys were derived from the Rietveld refinement of the temperature-dependent neutron diffraction data, while those of the x = 0.01 and 0.02 alloys were from the temperature-dependent X-ray diffraction data. All of the alloys show similar structural variations across the FM-to-PM transition, i.e. a decrease in lattice parameter *a* and an increase in lattice parameter *c*. With an increase in the Mo content, the relative changes in lattice parameters at the magnetoelastic transition are considerably reduced. For instance, the Mo-free alloy shows a relative change of 1.27% in lattice parameter *a* and a relative change of 2.73% in *c*, while the relative changes are significantly reduced to 0.79% and 1.71%, respectively in the x = 0.04 alloy. Consequently, the substitution of Fe by Mo in the $(Mn,Fe)_2(P,Si)$ alloys leads to improved structural compatibility between the PM and FM phases across the magnetoelastic transition.

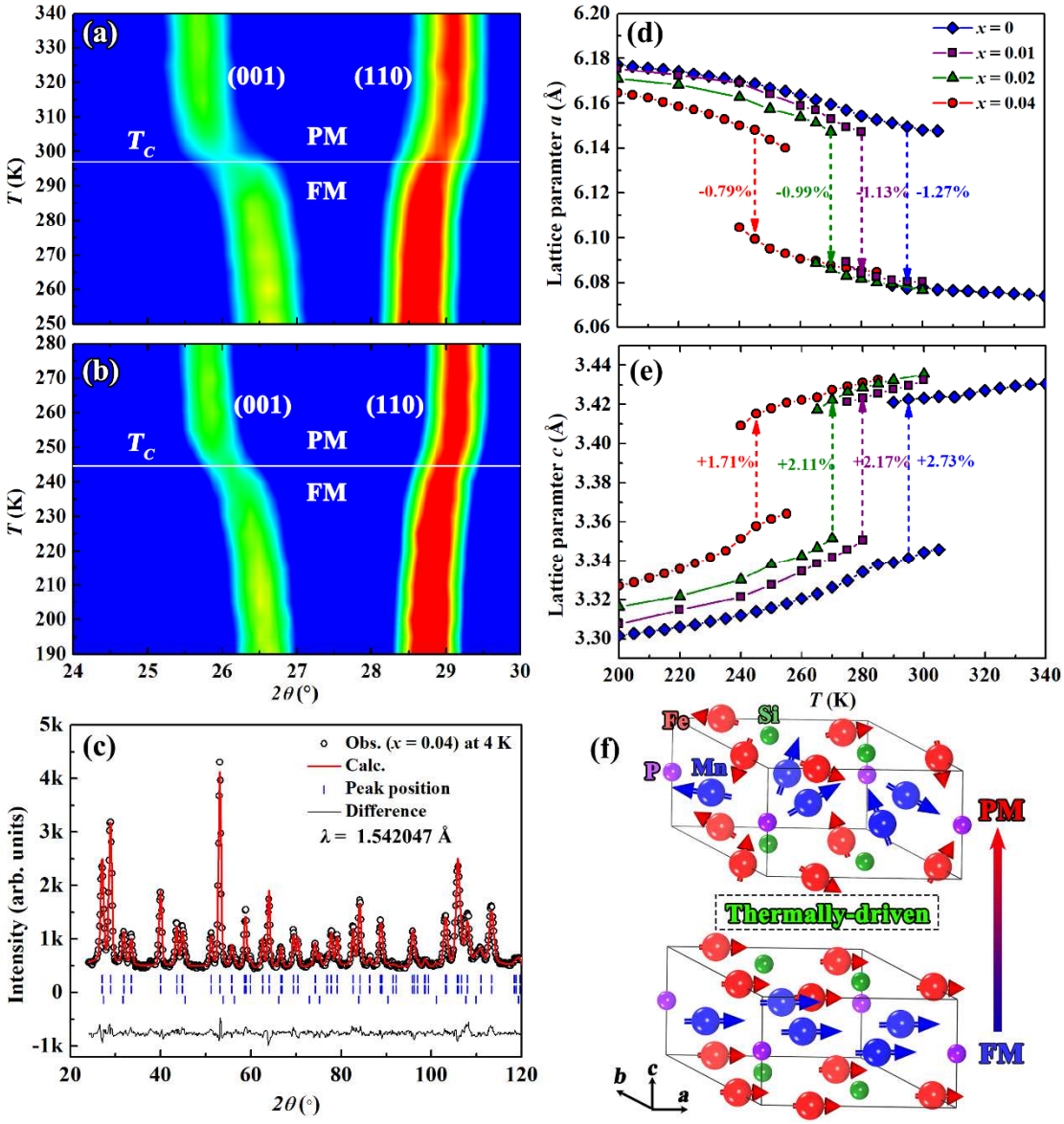

Fig. 6. Contour plots of the temperature-dependent neutron diffraction patterns for the $Mn_{1.15}Fe_{0.80-x}Mo_xP_{0.45}Si_{0.55}$ alloys with x = 0 (a) and 0.04 (b). (c) Rietveld refinement of the neutron diffraction pattern collected at T = 4 K in zero magnetic field for the $Mn_{1.15}Fe_{0.76}Mo_{0.04}P_{0.45}Si_{0.55}$ alloy. Vertical lines indicate the peak positions (from top to bottom) of the nuclear structure of the $(Mn,Fe)_2(P,Si)$ phase, the magnetic structure of the $(Mn,Fe)_2(P,Si)$ phase, and the Fe_3Si-type secondary phase, respectively. Thermal evolution of the lattice parameters a (d) and c (e) for the $Mn_{1.15}Fe_{0.80-x}Mo_xP_{0.45}Si_{0.55}$ alloys. Note that the lattice parameters of the x = 0 and 0.04 alloys were derived from temperature-dependent neutron diffraction patterns, while those of the x = 0.01 and 0.02 alloys were derived from temperature-dependent X-ray diffraction patterns. (f) Schematic illustration of the thermally-induced magnetoelastic transition in $(Mn,Fe)_2(P,Si)$ alloys.

3.6 Mechanism of the enhanced reversibility

A higher structural compatibility between the parent and the product phases has been proven to exhibit a better reversibility of the martensitic transformation in NiTi-based shape

memory alloys [23], NiMn-based Heusler alloys [24-26] and MnNiGe-based alloys [27]. The reduction in the thermal/magnetic hysteresis of the magnetoelastic transition in the $(Mn,Fe)_2(P,Si)$ alloys (see Fig. 1) can also be attributed to the improved structural compatibility after Mo substitution. Our previous neutron diffraction [42] and *in situ* TEM observations [16] revealed nucleation and growth processes of the magnetoelastic transition in the $(Mn,Fe)_2(P,Si)$ alloys. The large lattice mismatch between the PM and FM phases will induce considerable elastic strains in the material, which enhance the energy barrier for nucleation and hence increase the hysteresis of the magnetoelastic transition. The transition-induced elastic strain energy U_e can be calculated by

$$U_e = \frac{1}{2}\sum_{ij} C_{ij} e_i e_j \tag{1}$$

where the C_{ij} (i, j = 1, 2, 3, 4, 5, 6) are the elastic constants and $e_{i,j}$ is the elastic strain. For a hexagonal system, the C_{ij} can be described by a matrix with 5 independent elements [53]:

$$C_{ij} = \begin{pmatrix} C_{11} & C_{12} & C_{13} & 0 & 0 & 0 \\ C_{12} & C_{11} & C_{13} & 0 & 0 & 0 \\ C_{13} & C_{13} & C_{33} & 0 & 0 & 0 \\ 0 & 0 & 0 & C_{44} & 0 & 0 \\ 0 & 0 & 0 & 0 & C_{44} & 0 \\ 0 & 0 & 0 & 0 & 0 & (C_{11}-C_{12})/2 \end{pmatrix} \tag{2}$$

The tensile strain within the *ab* plane is $e_1 = e_2 = \Delta a/a$ and along the *c* axis $e_3 = \Delta c/c$. Combining Eqs. (1) - (2) and neglecting the shear strains, the elastic strain energy U_e induced across the magnetoelastic transition of the $(Mn,Fe)_2(P,Si)$ alloys can be estimated by

$$U_e = (C_{11} + C_{12})e_1^2 + 2C_{13}e_1e_3 + \frac{1}{2}C_{33}e_3^2 \tag{3}$$

Taking the elastic constants reported by Roy *et al.* [54] and the elastic strain ($\Delta a/a$ and $\Delta c/c$ values at T_C) from the literature [55-60], we can calculate the elastic strain energy U_e at T_C of the $(Mn,Fe)_2(P,Si)$ alloys with different compositions based on Eq. (3). Fig. 7 shows the relationship between the elastic strain energy and the thermal hysteresis for various $(Mn,Fe)_2(P,Si)$ alloys. This Ashby-like plot clearly demonstrates that the thermal hysteresis of the $(Mn,Fe)_2(P,Si)$ alloys can be minimized by reducing the transition-induced elastic strain energy. This strategy may also be applicable to other magnetoelastic materials like $La(Fe,Si)_{13}$ [5, 6], FeRh [61] and Eu_2In [62] since the elastic strain energy plays a similar role in the transition.

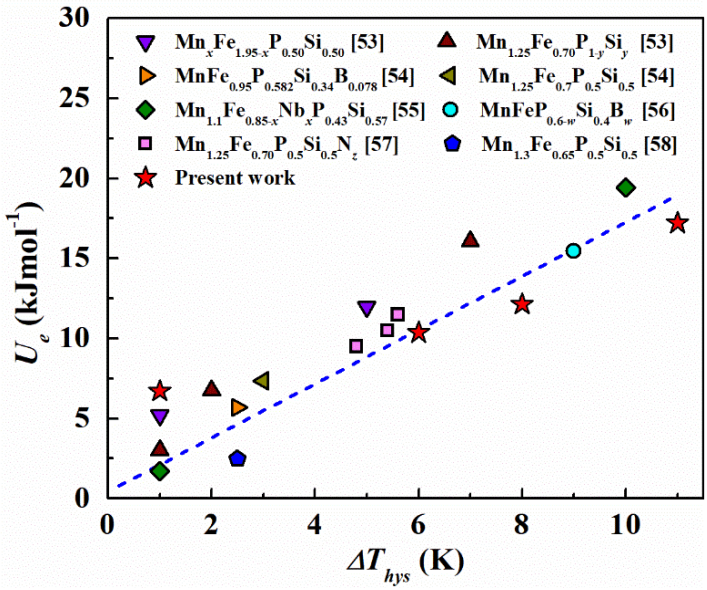

Fig. 7. Ashby-like plot demonstrating the relationship between the elastic strain energy U_e at T_C and the thermal hysteresis ΔT_{hys} for the $(Mn,Fe)_2(P,Si)$ alloys. The dashed line is a guide to the eyes.

3.7 Mechanism of the tunable transition temperature

Giant MCE is usually observed in a narrow temperature range around the T_C of the magnetoelastic transition. To facilitate wide temperature spans in magnetic refrigerators, multi-layered regenerators have been proposed, which require stacks of magnetocaloric materials with gradually varying T_C values. The T_C of the $(Mn,Fe)_2(P,Si)$ alloys can easily be tuned via compositional variations, e.g. metal- and nonmetal-element substitution [57, 63-66], as well as light element additions [46, 67, 68], which are desirable for fabricating multi-layered regenerators. However, the tuning mechanism of T_C in the $(Mn,Fe)_2(P,Si)$ alloys is still not well understood. High-resolution X-ray diffraction reveals an electron-density redistribution across the magnetoelastic transition of the $(Mn,Fe)_2(P,Si)$ alloys [69]. DFT calculations suggest a partial quenching of the Fe moment in addition to the order-disorder transition of the spin arrangement at the magnetoelastic transition [4, 69]. Our temperature-dependent neutron diffraction in Fig. 6 indicates significant lattice distortions accompanying the magnetoelastic transition. Consequently, the magnetoelastic transition in the $(Mn,Fe)_2(P,Si)$ alloys is associated with strong electron-spin-lattice coupling.

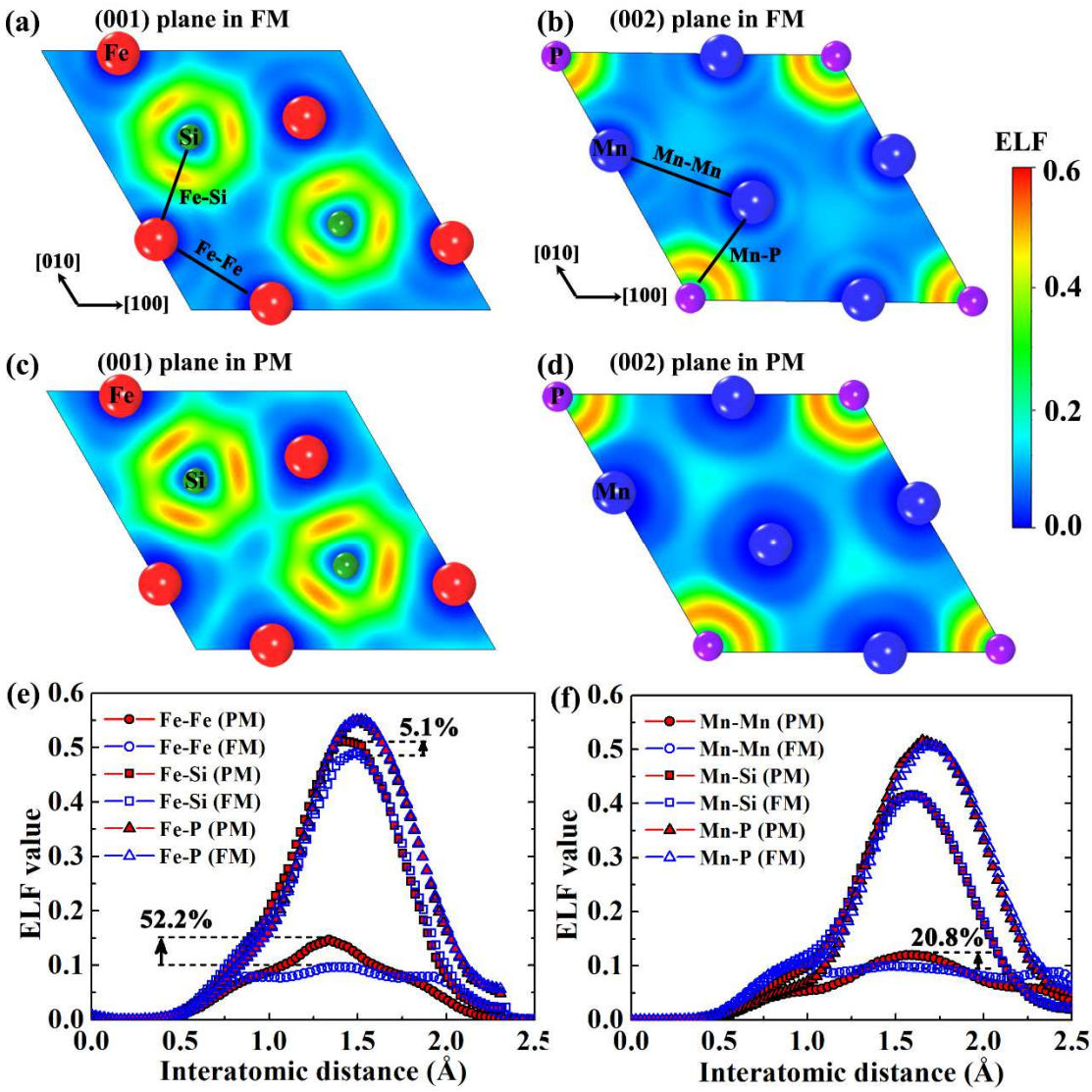

Fig. 8. Calculated ELF contour maps on the Fe-Si and Mn-P layers in (a-b) the FM and (c-d) the PM states of the $(Mn,Fe)_2(P,Si)$ alloys. Line profiles of the ELF values between (e) Fe and its nearest neighbors and (f) between Mn and its nearest neighbors. The stoichiometry of $MnFeP_{1/3}Si_{2/3}$ is assumed in the supercell for simplicity of the calculations.

In the $(Mn,Fe)_2(P,Si)$ alloys, the Fe-Si layer (i.e. the (001) lattice plane) and the Mn-P layer (i.e. the (002) lattice plane) are packed alternatively along the *c* axis of the hexagonal structure. Fig. 8 presents the calculated ELF contour maps on the Fe-Si and Mn-P layers in the FM (Figs. 8(a-b)) and PM (Figs. 8(c-d)) states. Higher ELF values correspond to more localized electrons, suggesting a stronger covalent bonding between the neighboring atoms. A noticeable difference in the ELF values between the FM and PM states can be observed around both the Fe and Mn atoms. To quantitatively study the subtle variations in the covalent bonding across the FM-PM transition, Figs. 8(e-f) compare the line profiles of the ELF values between the PM and FM

states. The most significant change in the ELF is found between the nearest Fe-Fe atoms, where the maximum ELF value in the PM state is 52.2% higher than that in the FM state. The maximum ELF values between the nearest Mn-Mn and Fe-Si atoms in the PM state are 20.8% and 5.1% higher than that in the FM state, respectively. Therefore, the ELF results suggest a significant enhancement of the covalent bonding between the neighboring atoms across the FM-to-PM transition, predominantly between the nearest Fe-Fe atoms.

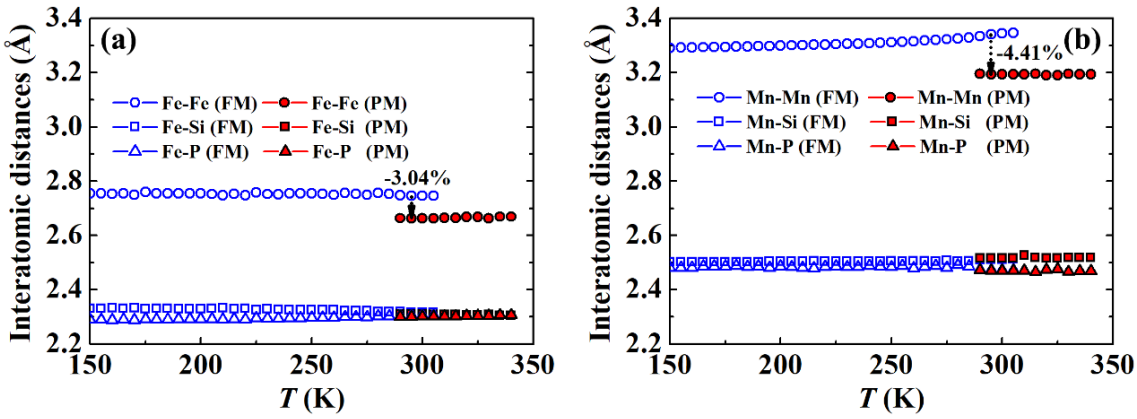

Fig. 9. Thermal evolution of interatomic distances extracted from neutron diffraction for the $Mn_{1.15}Fe_{0.80}P_{0.45}Si_{0.55}$ alloy. The errors on the refined distances are smaller than the symbol size.

The enhancement in the covalent bonding originates from a considerable shortening of the nearest Fe-Fe distance across the FM-to-PM transition, as shown in Fig. 9(a). Although the change in the Fe-Fe distance is slightly smaller than that in the Mn-Mn distance at the transition, the enhancement in the covalent bonding is more pronounced in the former. This may be due to the shorter Fe-Fe distances (≈ 2.7 Å) compared to the Mn-Mn distances (> 3.2 Å) in both FM and PM states, which leads to a stronger sensitivity of the Fe-Fe covalent bonding to the bond distance. The shorter Fe-Fe distance in the PM state may cause a larger overlap of the 3*d* orbitals between the neighboring Fe atoms, leading to a weaker exchange splitting between the majority and minority 3*d* band and hence a partial quenching of the Fe moment in the PM state. Consequently, the magnetoelastic transition in the $(Mn,Fe)_2(P,Si)$ alloys is dominated by the competition between the covalent bonding and the ferromagnetic exchange coupling. Rising the temperature of the system will boost thermal fluctuations and destroy the ferromagnetic exchange coupling between the neighboring moments, which favors the covalent bonding and thus the PM state. As a result, a thermally-driven magnetoelastic transition is observed in the

$(Mn,Fe)_2(P,Si)$ alloys (illustrated in Fig. 6(f)). Alternatively, applying an external field will strengthen the ferromagnetic exchange coupling in the $(Mn,Fe)_2(P,Si)$ system, which favors the FM state and can thereby induce the magnetoelastic transition (illustrated in Fig. 2(b)).

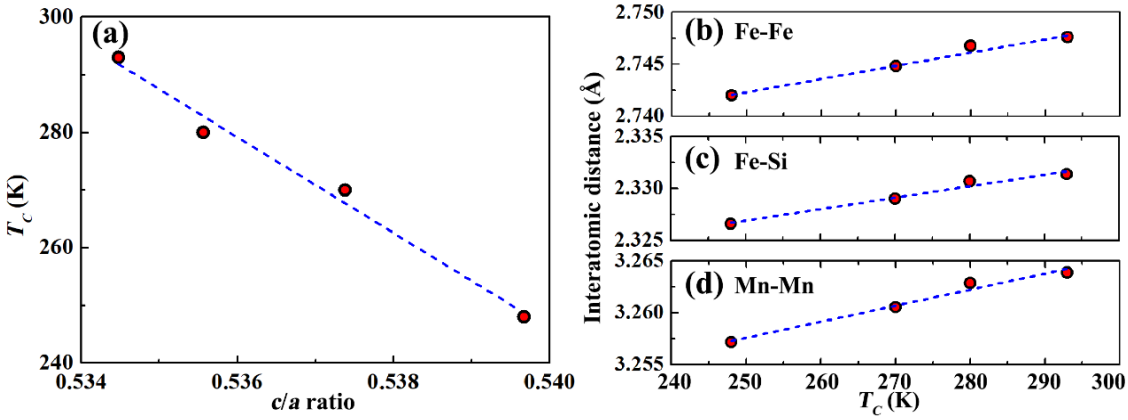

Fig. 10. (a) The relationship between the T_C of the FM-to-PM transition and the c/a ratio of the hexagonal structure at 200 K for the $Mn_{1.15}Fe_{0.80-x}Mo_xP_{0.45}Si_{0.55}$ alloys. (b-d) The nearest interatomic distances at 200 K with respect to the T_C. The errors on the c/a ratio and the interatomic distances are smaller than the symbol size.

Apart from the thermal and magnetic stimuli, the direct change of bond distance via compositional variations can also effectively manipulate the balance between covalent bonding and ferromagnetic exchange coupling. Here we take the Mo substitution for Fe as an example to elucidate the tuning mechanism of the T_C via compositional variations in the $(Mn,Fe)_2(P,Si)$ alloys. Fig. 10(a) shows the relationship between the T_C and the c/a ratio of the hexagonal structure for the $Mn_{1.15}Fe_{0.80-x}Mo_xP_{0.45}Si_{0.55}$ alloys. Note that the c/a ratio was derived from the Rietveld refinement of the neutron and X-ray diffraction data at 200 K, where all the samples were in the FM state. Interestingly, the T_C value decreases almost linearly with the c/a ratio of the FM phase, suggesting an underlying coupling between the structural parameters and the magnetic transition. Figs. 10(b-d) plot the nearest Fe-Fe, Fe-Si and Mn-Mn distances with respect to T_C. Obviously, the $Mn_{1.15}Fe_{0.80-x}Mo_xP_{0.45}Si_{0.55}$ alloy with a higher T_C corresponds to larger Fe-Fe, Fe-Si and Mn-Mn interatomic distances in the FM state. This can also be understood from the competition between covalent bonding and ferromagnetic exchange coupling. The covalent bonding is weakened with the increasing interatomic distances, which stabilizes the FM state and thus pushes the T_C to higher temperatures. Tuning the T_C of the $(Mn,Fe)_2(P,Si)$ alloys via other metal- and nonmetal-element substitution [57, 63-66], as well

as light element addition [46, 67, 68] can be explained by the competition between covalent bonding and ferromagnetic exchange coupling. The proposed tuning mechanism of the magnetoelastic transition is expected to be applicable to other magnetoelastic materials like $La(Fe,Si)_{13}$ [5, 6], FeRh [61] and Eu_2In [62], where the magnetoelastic transition is also dominated by the strong electron-spin-lattice coupling.

4. Conclusions

In summary, we found a significant enhancement of the reversible magnetocaloric properties in $(Mn,Fe)_2(P,Si)$ alloys by a partial substitution of Fe by Mo. The reversible adiabatic temperature change is increased significantly in the $Mn_{1.15}Fe_{0.76}Mo_{0.04}P_{0.45}Si_{0.55}$ alloy, compared to the Mo-free alloy. To uncover the underlying mechanism of the enhanced reversible magnetocaloric properties, we performed comprehensive experimental (TEM and *in situ* neutron diffraction) and theoretical (DFT calculations) studies. *In situ* neutron diffraction in a cyclic magnetic field revealed a very small irreversible contribution (≈ 5.3%) in the magnetoelastic transition of the $Mn_{1.15}Fe_{0.76}Mo_{0.04}P_{0.45}Si_{0.55}$ alloy. The high reversibility in the $Mn_{1.15}Fe_{0.76}Mo_{0.04}P_{0.45}Si_{0.55}$ alloy also manifests itself by a small thermal hysteresis of 1 K. Based on the relative changes in the lattice parameters across the magnetoelastic transition, we calculated the transition-induced elastic strain energy, which shows a generalized relationship with the thermal hysteresis in the $(Mn,Fe)_2(P,Si)$ family. As a result, the enhanced reversible magnetocaloric properties after the Mo substitution can be attributed to the reduced transition-induced elastic strain energy and the resultant high reversibility of the magnetoelastic transition. Additionally, the ELF results suggest a significant strengthening of the covalent bonding between the nearest Fe-Fe atoms across the FM-to-PM transition, which is coupled to a partial quenching of the Fe moment as well as a shortening of the nearest Fe-Fe distance. Manipulating the magnetoelastic transition via the thermal and magnetic stimuli as well as compositional variations essentially relies on the tailoring of the strong electron-spin-lattice coupling in the $(Mn,Fe)_2(P,Si)$ alloys. The strategy for improving reversible magnetocaloric properties and the mechanism of tuning the magnetoelastic transition proposed in the present work are crucial to optimize the current material systems and to boost the search for promising magnetocaloric materials for magnetic refrigeration applications.

Acknowledgements

This work was supported by the National Natural Science Foundation of China (grant numbers 51801102, U1832191, 12004179), the Natural Science Foundation of Jiangsu Province (grant number BK20180491, BK20180418), and the Open Fund of Large Facilities in Nanjing University of Science and Technology. This work is based on NPD experiments performed at Australian Nuclear Science and Technology Organization (ANSTO) in Australia. The authors thank Anton Lefering for the technical support on the adiabatic temperature change measurements.

Reference

[1] A. Kitanovski, Energy applications of magnetocaloric materials, Adv. Energy Mater. 10 (2020) 1903741.

[2] T. Gottschall, K.P. Skokov, M. Fries, A. Taubel, I. Radulov, F. Scheibel, D. Benke, S. Riegg, O. Gutfleisch, Making a cool choice: the materials library of magnetic refrigeration, Adv. Energy Mater. 9 (2019) 1901322.

[3] V.K. Pecharsky, K.A. Gschneidner Jr, Giant magnetocaloric effect in $Gd_5(Si_2Ge_2)$, Phys. Rev. Lett. 78 (1997) 4494-4497.

[4] N.H. Dung, Z.Q. Ou, L. Caron, L. Zhang, D.T.C. Thanh, G.A. de Wijs, R.A. de Groot, K.H.J. Buschow, E. Brück, Mixed magnetism for refrigeration and energy conversion, Adv. Energy Mater. 1 (2011) 1215-1219.

[5] F.X. Hu, B.G. Shen, J.R. Sun, Z.H. Cheng, G.H. Rao, X.X. Zhang, Influence of negative lattice expansion and metamagnetic transition on magnetic entropy change in the compound $LaFe_{11.4}Si_{1.6}$, Appl. Phys. Lett. 78 (2001) 3675-3677.

[6] A. Fujita, S. Fujieda, Y. Hasegawa, K. Fukamichi, Itinerant-electron metamagnetic transition and large magnetocaloric effects in $La(Fe_xSi_{1-x})_{13}$ compounds and their hydrides, Phys. Rev. B 67 (2003) 104416.

[7] E.K. Liu, W.H. Wang, L. Feng, W. Zhu, G.J. Li, J. Chen, H.W. Zhang, G.H. Wu, C.B. Jiang, H.B. Xu, F. de Boer, Stable magnetostructural coupling with tunable magnetoresponsive effects in hexagonal ferromagnets, Nat. Commun. 3 (2012) 873.

[8] Y. Taguchi, H. Sakai, D. Choudhury, Magnetocaloric materials with multiple instabilities,

Adv. Mater. 29 (2017) 1606144.

[9] T. Krenke, E. Duman, M. Acet, E.F. Wassermann, X. Moya, L. Manosa, A. Planes, Inverse magnetocaloric effect in ferromagnetic Ni-Mn-Sn alloys, Nat. Mater. 4 (2005) 450-454.

[10] J. Liu, T. Gottschall, K.P. Skokov, J.D. Moore, O. Gutfleisch, Giant magnetocaloric effect driven by structural transitions, Nat. Mater. 11 (2012) 620-626.

[11] T. Gottschall, K.P. Skokov, B. Frincu, O. Gutfleisch, Large reversible magnetocaloric effect in Ni-Mn-In-Co, Appl. Phys. Lett. 106 (2015) 021901.

[12] O. Gutfleisch, T. Gottschall, M. Fries, D. Benke, I. Radulov, K.P. Skokov, H. Wende, M. Gruner, M. Acet, P. Entel, M. Farle, Mastering hysteresis in magnetocaloric materials, Phil. Trans. R. Soc. A 374 (2016) 20150308.

[13] L.D. Landau, On the theory of phase transitions. I, Zh. Eksp. Teor. Fiz. 7 (1937) 19-32.

[14] A.M.G. Carvalho, A.A. Coelho, S. Gama, F.C.G. Gandra, P.J. von Ranke, N.A. de Oliveira, Investigation of the first-order metamagnetic transitions and the colossal magnetocaloric effect using a Landau expansion applied to MnAs compound, Eur. Phys. J. B 68 (2009) 67-72.

[15] N.H. van Dijk, Landau model evaluation of the magnetic entropy change in magnetocaloric materials, J. Magn. Magn. Mater. 529 (2021) 167871.

[16] X.F. Miao, H. Sepehri-Amin, K. Hono, Structural origin of hysteresis for hexagonal $(Mn,Fe)_2(P,Si)$ magneto-caloric compound, Scr. Mater. 138 (2017) 96-99.

[17] M. Fries, L. Pfeuffer, E. Bruder, T. Gottschall, S. Ener, L.V.B. Diop, T. Gröb, K.P. Skokov, O. Gutfleisch, Microstructural and magnetic properties of Mn-Fe-P-Si (Fe_2P-type) magnetocaloric compounds, Acta Mater. 132 (2017) 222-229.

[18] A. Bartok, M. Kustov, L.F. Cohen, A. Pasko, K. Zehani, L. Bessais, F. Mazaleyrat, M. LoBue, Study of the first paramagnetic to ferromagnetic transition in as prepared samples of Mn-Fe-P-Si magnetocaloric compounds prepared by different synthesis routes, J. Magn. Magn. Mater. 400 (2016) 333-338.

[19] K. Morrison, J. Moore, K. Sandeman, A. Caplin, L. Cohen, Capturing first- and second-order behavior in magnetocaloric $CoMnSi_{0.92}Ge_{0.08}$, Phys. Rev. B 79 (2009) 134408.

[20] L. Morellon, Z. Arnold, C. Magen, C. Ritter, O. Prokhnenko, Y. Skorokhod, P.A. Algarabel, M.R. Ibarra, J. Kamarad, Pressure enhancement of the giant magnetocaloric effect in

$Tb_5Si_2Ge_2$, Phys. Rev. Lett. 93 (2004) 137201.

[21] H. Zhang, B.G. Shen, Z.Y. Xu, X.Q. Zheng, J. Shen, F.X. Hu, J.R. Sun, Y. Long, Reduction of hysteresis loss and large magnetocaloric effect in the C- and H-doped $La(Fe,Si)_{13}$ compounds around room temperature, J. Appl. Phys. 111 (2012) 07A909.

[22] K. Bhattacharya, S. Conti, G. Zanzotto, J. Zimmer, Crystal symmetry and the reversibility of martensitic transformations, Nature 428 (2004) 55-59.

[23] J. Cui, Y.S. Chu, O.O. Famodu, Y. Furuya, J. Hattrick-Simpers, R.D. James, A. Ludwig, S. Thienhaus, M. Wuttig, Z. Zhang, I. Takeuchi, Combinatorial search of thermoelastic shape-memory alloys with extremely small hysteresis width, Nat. Mater. 5 (2006) 286-290.

[24] Y.H. Qu, D.Y. Cong, S.H. Li, W.Y. Gui, Z.H. Nie, M.H. Zhang, Y. Ren, Y.D. Wang, Simultaneously achieved large reversible elastocaloric and magnetocaloric effects and their coupling in a magnetic shape memory alloy, Acta Mater. 151 (2018) 41-55.

[25] D.Y. Cong, L. Huang, V. Hardy, D. Bourgault, X.M. Sun, Z.H. Nie, M.G. Wang, Y. Ren, P. Entel, Y.D. Wang, Low-field-actuated giant magnetocaloric effect and excellent mechanical properties in a NiMn-based multiferroic alloy, Acta Mater. 146 (2018) 142-151.

[26] Y.H. Qu, D.Y. Cong, X.M. Sun, Z.H. Nie, W.Y. Gui, R.G. Li, Y. Ren, Y.D. Wang, Giant and reversible room-temperature magnetocaloric effect in Ti-doped Ni-Co-Mn-Sn magnetic shape memory alloys, Acta Mater. 134 (2017) 236-248.

[27] J. Liu, Y. Gong, Y. You, X. You, B. Huang, X. Miao, G. Xu, F. Xu, E. Brück, Giant reversible magnetocaloric effect in MnNiGe-based materials: Minimizing thermal hysteresis via crystallographic compatibility modulation, Acta Mater. 174 (2019) 450-458.

[28] C. Chluba, W. Ge, R. Lima de Miranda, J. Strobel, L. Kienle, E. Quandt, M. Wuttig, Ultralow-fatigue shape memory alloy films, Science 348 (2015) 1004-1007.

[29] Y. Liu, X. Fu, Q. Yu, M. Zhang, J. Liu, Significant reduction of phase-transition hysteresis for magnetocaloric $(La_{1-x}Ce_x)_2Fe_{11}Si_2H$ alloys by microstructural manipulation, Acta Mater. 207 (2021) 116687.

[30] V. Provenzano, A.J. Shapiro, R.D. Shull, Reduction of hysteresis losses in the magnetic refrigerant $Gd_5Ge_2Si_2$ by the addition of iron, Nature 429 (2004) 853-857.

[31] H. Sepehri-Amin, A. Taubel, T. Ohkubo, K.P. Skokov, O. Gutfleisch, K. Hono, Microstructural origin of hysteresis in Ni-Mn-In based magnetocaloric compounds, Acta Mater. 147 (2018) 342-349.

[32] H. Hou, E. Simsek, T. Ma, N.S. Johnson, S. Qian, C. Cissé, D. Stasak, N. Al Hasan, L. Zhou, Y. Hwang, R. Radermacher, V.I. Levitas, M.J. Kramer, M.A. Zaeem, A.P. Stebner, R.T. Ott, J. Cui, I. Takeuchi, Fatigue-resistant high-performance elastocaloric materials made by additive manufacturing, Science 366 (2019) 1116-1121.

[33] H. Chen, Y.-D. Wang, Z. Nie, R. Li, D. Cong, W. Liu, F. Ye, Y. Liu, P. Cao, F. Tian, X. Shen, R. Yu, L. Vitos, M. Zhang, S. Li, X. Zhang, H. Zheng, J.F. Mitchell, Y. Ren, Unprecedented non-hysteretic superelasticity of [001]-oriented NiCoFeGa single crystals, Nat. Mater. 19 (2020) 712-718.

[34] M. Trassinelli, M. Marangolo, M. Eddrief, V.H. Etgens, V. Gafton, S. Hidki, E. Lacaze, E. Lamour, C. Prigent, J.P. Rozet, S. Steydli, Y. Zheng, D. Vernhet, Suppression of the thermal hysteresis in magnetocaloric MnAs thin film by highly charged ion bombardment, Appl. Phys. Lett. 104 (2014) 081906.

[35] R. Niemann, S. Hahn, A. Diestel, A. Backen, L. Schultz, K. Nielsch, M.F.X. Wagner, S. Fähler, Reducing the nucleation barrier in magnetocaloric Heusler alloys by nanoindentation, APL Mater. 4 (2016) 064101.

[36] F.X. Hu, L. Chen, J. Wang, L.F. Bao, J.R. Sun, B.G. Shen, Particle size dependent hysteresis loss in $La_{0.7}Ce_{0.3}Fe_{11.6}Si_{1.4}C_{0.2}$ first-order systems, Appl. Phys. Lett. 100 (2012) 072403.

[37] A. Waske, L. Giebeler, B. Weise, A. Funk, M. Hinterstein, M. Herklotz, K. Skokov, S. Fähler, O. Gutfleisch, J. Eckert, Asymmetric first-order transition and interlocked particle state in magnetocaloric $La(Fe,Si)_{13}$, Phys. Status Solidi RRL 9 (2015) 136-140.

[38] J. Lyubina, R. Schafer, N. Martin, L. Schultz, O. Gutfleisch, Novel design of $La(Fe,Si)_{13}$ alloys towards high magnetic refrigeration performance, Adv. Mater. 22 (2010) 3735.

[39] E. Lovell, A.M. Pereira, A.D. Caplin, J. Lyubina, L.F. Cohen, Dynamics of the first-order metamagnetic transition in magnetocaloric $La(Fe,Si)_{13}$: reducing hysteresis, Adv. Energy Mater. 5 (2015) 1401639.

[40] J.D. Moore, K. Morrison, K.G. Sandeman, M. Katter, L.F. Cohen, Reducing extrinsic

hysteresis in first-order $La(Fe,Co,Si)_{13}$ magnetocaloric systems, Appl. Phys. Lett. 95 (2009) 252504.

[41] Y. Liu, L.C. Phillips, R. Mattana, M. Bibes, A. Barthelemy, B. Dkhil, Large reversible caloric effect in FeRh thin films via a dual-stimulus multicaloric cycle, Nat. Commun. 7 (2016).

[42] X.F. Miao, L. Caron, J. Cedervall, P.C.M. Gubbens, P. Dalmas de Réotier, A. Yaouanc, F. Qian, A.R. Wildes, H. Luetkens, A. Amato, N.H. van Dijk, E. Brück, Short-range magnetic correlations and spin dynamics in the paramagnetic regime of $(Mn,Fe)_2(P,Si)$, Phys. Rev. B 94 (2016) 014426.

[43] N.H. Dung, Moment formation and giant magnetocaloric effects in hexagonal Mn-Fe-P-Si compounds, Ph.D. dissertation, Delft University of Technology, Delft, 2012.

[44] A.J. Studer, M.E. Hagen, T.J. Noakes, Wombat: the high-intensity powder diffractometer at the OPAL reactor, Physica B 385-386 (2006) 1013-1015.

[45] J. Rodriguez-Carvajal, Recent advances in magnetic structure determination by neutron powder diffraction, Physica B 192 (1993) 55-69.

[46] F. Guillou, G. Porcari, H. Yibole, N.H. van Dijk, E. Brück, Taming the first-order transition in giant magnetocaloric materials, Adv. Mater 26 (2014) 2671.

[47] H. Yibole, F. Guillou, L. Zhang, N.H. van Dijk, E. Brück, Direct measurement of the magnetocaloric effect in MnFe(P,X) (X= As, Ge, Si) materials, J. Phys. D: Appl. Phys. 47 (2014) 075002.

[48] G. Kresse, J. Furthmuller, Efficient iterative schemes for ab initio total-energy calculations using a plane-wave basis set, Phys. Rev. B 54 (1996) 11169.

[49] A.D. Becke, K.E. Edgecombe, A simple measure of electron localization in atomic and molecular systems, J. Chem. Phys. 92 (1990) 5397-5403.

[50] L. Caron, Z.Q. Ou, T.T. Nguyen, D.T. Cam Thanh, O. Tegus, E. Brück, On the determination of the magnetic entropy change in materials with first-order transitions, J. Magn. Magn. Mater. 321 (2009) 3559-3566.

[51] J. Gschneidner, K. A., V.K. Pecharsky, A.O. Tsokol, Recent developments in magnetocaloric materials, Rep. Prog. Phys. 68 (2005) 1479-1539.

[52] X.F. Miao, L. Caron, P. Roy, N.H. Dung, L. Zhang, W.A. Kockelmann, R.A. de Groot,

N.H. van Dijk, E. Brück, Tuning the phase transition in transition-metal-based magnetocaloric compounds, Phys. Rev. B 89 (2014) 174429.

[53] J.F. Nye, Physical Properties of Crystals: Their Pepresentation by Tensors and Matrices, Oxford University Press, Oxford, UK, 1985.

[54] P. Roy, E. Torun, R.A. de Groot, Effect of doping and elastic properties in $(Mn,Fe)_2(Si,P)$, Phys. Rev. B 93 (2016) 094110.

[55] N.H. Dung, L. Zhang, Z.Q. Ou, E. Brück, Magnetoelastic coupling and magnetocaloric effect in hexagonal Mn-Fe-P-Si compounds, Scr. Mater. 67 (2012) 975-978.

[56] F. Guillou, H. Yibole, N.H. van Dijk, L. Zhang, V. Hardy, E. Brück, About the mechanical stability of MnFe(P,Si,B) giant-magnetocaloric materials, J. Alloys Compd. 617 (2014) 569-574.

[57] S.Y. Hu, X.F. Miao, J. Liu, Z.Q. Ou, M.Q. Cong, O. Haschuluu, Y.Y. Gong, F. Qian, Y.R. You, Y.J. Zhang, F. Xu, E. Brück, Small hysteresis and giant magnetocaloric effect in Nb-substituted $(Mn,Fe)_2(P,Si)$ alloys, Intermetallics 114 (2019) 106602.

[58] M. Maschek, X. You, M.F.J. Boeije, D. Chernyshov, N.H. van Dijk, E. Brück, Charge redistribution and the magnetoelastic transition across the first-order magnetic transition in $(Mn,Fe)_2(P,Si,B)$, Phys. Rev. B 98 (2018) 224413.

[59] N.V. Thang, X.F. Miao, N.H. van Dijk, E. Brück, Structural and magnetocaloric properties of $(Mn,Fe)_2(P,Si)$ materials with added nitrogen, J. Alloys Compd. 670 (2016) 123-127.

[60] A. Pasko, A. Bartok, K. Zehani, L. Bessais, F. Mazaleyrat, M. LoBue, X-ray diffraction analysis of the magnetoelastic phase transition in the Mn-Fe-P-Si magnetocaloric alloy, AIP Adv. 6 (2016) 056204.

[61] G. Shirane, R. Nathans, C.W. Chen, Magnetic moments and unpaired spin densities in the Fe-Rh alloys, Phys. Rev. 134 (1964) A1547-A1553.

[62] F. Guillou, A.K. Pathak, D. Paudyal, Y. Mudryk, F. Wilhelm, A. Rogalev, V.K. Pecharsky, Non-hysteretic first-order phase transition with large latent heat and giant low-field magnetocaloric effect, Nat. Commun. 9 (2018) 2925.

[63] J. Lai, B. Huang, X. Miao, N. Van Thang, X. You, M. Maschek, L. van Eijck, D. Zeng, N. van Dijk, E. Brück, Combined effect of annealing temperature and vanadium substitution for mangetocaloric $Mn_{1.2-x}V_xFe_{0.75}P_{0.5}Si_{0.5}$ alloys, J. Alloys Compd. 803 (2019) 671-677.

[64] Z.Q. Ou, N.H. Dung, L. Zhang, L. Caron, E. Torun, N.H. van Dijk, O. Tegus, E. Brück, Transition metal substitution in Fe_2P-based $MnFe_{0.95}P_{0.50}Si_{0.50}$ magnetocaloric compounds, J. Alloys Compd. 730 (2018) 392-398.

[65] H. Wada, K. Nakamura, K. Katagiri, T. Ohnishi, K. Yamashita, A. Matsushita, Tuning the Curie temperature and thermal hysteresis of giant magnetocaloric $(MnFe)_2PX$ (X = Ge and Si) compounds by the Ru substitution, Jpn. J. Appl. Phys. 53 (2014) 063001.

[66] D. Liu, M. Yue, J. Zhang, T. McQueen, J. Lynn, X. Wang, Y. Chen, J. Li, R. Cava, X. Liu, Z. Altounian, Q. Huang, Origin and tuning of the magnetocaloric effect in the magnetic refrigerant $Mn_{1.1}Fe_{0.9}(P_{0.8}Ge_{0.2})$, Phys. Rev. B 79 (2009) 014435.

[67] X.F. Miao, N.V. Thang, L. Caron, H. Yibole, R.I. Smith, N.H. van Dijk, E. Brück, Tuning the magnetoelastic transition in $(Mn,Fe)_2(P,Si)$ by B, C, and N doping, Scr. Mater. 124 (2016) 129-132.

[68] Q. Zhou, Z.G. Zheng, W.H. Wang, L. Lei, A. He, D.C. Zeng, Carbon doping in the $Mn_{1.15}Fe_{0.80}P_{0.50}Si_{0.50}$ materials: structure, phase transition and magnetocaloric properties, Intermetallics 106 (2019) 94-99.

[69] M.F.J. Boeije, P. Roy, F. Guillou, H. Yibole, X.F. Miao, L. Caron, D. Banerjee, N.H. van Dijk, R.A. de Groot, E. Brück, Efficient room-temperature cooling with magnets, Chem. Mater. 28 (2016) 4901-4905.